Scripta Materialia 110 (2016) 65–69

Contents lists available at ScienceDirect

Scripta Materialia

journal homepage: www.elsevier.com/locate/scriptamat

Elastic and plastic Poisson's ratios of nanoporous gold

Lukas Lührs [a,*], Celal Soyarslan [b], Jürgen Markmann [c,a], Swantje Bargmann [b,c], Jörg Weissmüller [a,c]

[a] Institute of Materials Physics and Technology, Hamburg University of Technology, Hamburg, Germany
[b] Institute of Continuum Mechanics and Material Mechanics, Hamburg University of Technology, Hamburg, Germany
[c] Institute of Materials Research, Materials Mechanics, Helmholtz-Zentrum Geesthacht, Geesthacht, Germany

ARTICLE INFO

Article history:
Received 28 July 2015
Accepted 4 August 2015
Available online 19 August 2015

Keywords:
Nanoporous metal
Mechanical properties
Nanostructure
Porous material
Finite element analysis

ABSTRACT

We explore the elastic and plastic Poisson's ratios, ν_E and ν_P, of nanoporous gold, using digital image correlation during compression experiments including load/unload segments. The two coefficients differ significantly, with ν_E independent of the ligament size, L, and with a trend for $\nu_P \propto L$ at not too large L. Disorder in the network of ligaments may explain why ν_E is smaller than predicted by lattice-based models. Finite element simulations, based on the Deshpande–Fleck constitutive law, validate the data analysis. The constitutive law captures work-hardening and transverse flow of nanoporous gold in good agreement with the experiment.

1. Introduction

Nanoporous gold (NPG) made by dealloying takes the form of macroscopic bodies that exhibit a uniform, bicontinuous network of nanoscale pores and solid "ligaments". The high degree of structural definition, the small lower limit of the structure size and the fact that annealing allows this size to be controlled between few and several hundred nanometers makes the material an attractive model system for studies of small-scale plasticity [1–4]. Experiments on fracture [5,6], indentation [7–9], compression [10–13] and tension [14–16] behavior exemplify the current interest in NPG. In this context it is noteworthy that models for the mechanical behavior of porous solids [17,18] and specifically NPG [19–21] differ in respect to their prediction for the transverse mechanical coupling during the elastic and plastic deformation, or even explicitly link the transverse strains to structural characteristics of the metal network [19,20]. Empirical studies of the transverse coupling may therefore provide a test for models of NPG.

Experimental studies of the *elastic* Poisson ratio, ν_E, are emerging, yet the distinction to the plastic transverse reaction is not always acknowledged and precise experimental studies of the *plastic* Poisson ratio, ν_P, are missing. Several studies assume the plastic transverse coupling in NPG to be analogous to that of macroporous metallic foams [17], suggesting ν_P near zero [2,7,8,22]. Studies using molecular dynamics and finite elements simulation support this assumption by presenting near zero or even negative values for ν_P under compressive loading [19–21]. Transverse strains measured ex situ after plastic deformation[11,13] indicate nonzero but small net plastic Poisson's ratio. Yet, the limited accuracy of these experiments does not afford a validation of models, nor is a possible variation of ν_P in response to the significant structure changes during the compression of the network resolved. As for ν_E, compression experiments find a value of 0.17 at 0.3% engineering strain [15], while reported values for tension loading are 0.15 [15] and 0.18 [6]. Again, the studies do not resolve a possible variation of the transverse response when the network geometry changes during plastic deformation.

Here, we present a study of the compressive deformation of npg to large plastic strain, using digital image correlation (DIC) and load/unload protocols to extract separately ν_E and ν_P at the various stages of plastic compression. We match the experiments through modeling the effective, macroscopic deformation behavior in the experimental geometry by finite-element-model (FEM) simulation. Besides removing possible artifacts from non-uniaxial loading, our FEM simulation also for the first time explores a constitutive model for the flow behavior of NPG. We find that the Deshpande–Fleck model [23], which is known to reproduce the mechanical behavior of classic metal foams with macroscopic cells, provides an excellent fit to the DIC data of NPG.

2. Experimental procedures

Cylindrical $Au_{25}Ag_{75}$ master alloy samples, 0.9 ± 0.05 mm in diameter and 1.8 ± 0.05 mm in length, were prepared according to Ref. [24]. Dealloying in 1 M $HClO_4$ used a potential of 0.75 V

* Corresponding author.
E-mail address: lukas.luehrs@tuhh.de (L. Lührs).

http://dx.doi.org/10.1016/j.scriptamat.2015.08.002
1359-6462/

vs. Ag/AgCl reference electrodes in the same solution (1.265 V vs. the standard hydrogen electrode). Residual silver was subsequently removed by polarization at 0.85 V in fresh electrolyte, followed by 20 potential cycles ranging from −0.4 to 1.1 V at a scan rate of 5 mV/s. Both, the polarization and the cyclic voltammetry steps were repeated once, ending at a final potential of 0.3 V to remove superficial oxygen [25]. The residual silver content, determined by energy-dispersive X-ray spectroscopy analysis, was found to be below 1 at.%. All samples exhibited an aspect ratio of 1.9 ± 0.1.

The above procedure yields mean ligament sizes, as identified by scanning electron microscopy, around 50 nm. By annealing a fraction of the samples in air at 300 °C the ligament size was increased to approximately 120 nm (10 min) and 180 nm (20 min). The mass density, as determined from the sample's mass and external dimensions, was 4.9±0.1, 5.4±0.1 and $5.5 \pm 0.1 \mathrm{g/cm^{-3}}$ for samples with ligament sizes of L = 50, 120 and 180 nm, respectively. The corresponding solid fractions emerged as 0.25±0.01, 0.27±0.01, 0.28±0.01, respectively.

Single loading and load/unload compression tests were performed using a universal testing machine (Zwick 1474) equipped with a DIC system (DaVis 8.2.0, LaVision), see Fig. 1. All tests were performed at a constant engineering strain rate of 10^{-4}/s, with a pre-load of 1 N at the beginning of the measurement. The elastic properties were determined during unloading at different deformation stages. Virtual strain gauges were placed on the sample surface to measure the strain in the axial direction, ε_a, and normal to it. For comparison with the FEM simulation, the transverse strain was measured in the sample center (ε_t^c) and close to the contact surfaces (ε_t^s).

The DIC output is engineering strain, which was converted to true strain where appropriate. Specifically, all Poisson's ratios in each state of plastic deformation were computed from *true* strain increments $\delta\varepsilon$ according to

$$\nu = -\frac{\delta\varepsilon_t^c}{\delta\varepsilon_a} \tag{1}$$

3. Simulation

As the constitutive equation for the effective macroscopic mechanical behavior of NPG, our modeling uses Deshpande and Fleck's self similar model [23], originally proposed for multiaxial closed cell metallic foams. It expresses the yield function Φ as the function of the (rotated Kirchhoff) stress $\boldsymbol{\tau}$ and the equivalent plastic strain ϵ_P by[1]

$$\Phi(\boldsymbol{\tau}, \epsilon_P) := \hat{\tau}(\boldsymbol{\tau}) - Y(\epsilon_P) \leq 0, \tag{2}$$

where $\hat{\tau}^2(\boldsymbol{\tau}) := [\tau_{eq}^2 + \alpha^2\tau_m^2]/[1 + [\alpha/3]^2]$ and with $\tau_{eq}^2 := 3/2\,\mathrm{dev}(\boldsymbol{\tau}) : \mathrm{dev}(\boldsymbol{\tau}), \tau_m := \mathrm{tr}(\boldsymbol{\tau})/3$. The parameter α defines the yield surface ellipticity. The plastic isotropic hardening is controlled by $Y(\epsilon_P)$ with

$$Y(\epsilon_P) := K\epsilon_P + \tau_\infty - [\tau_\infty - \tau_0]\exp(-m[\epsilon_P]^n), \tag{3}$$

where $K, \tau_\infty, \tau_0, m$ and n are corresponding material parameters. This model allows direct control of the plastic Poisson's ratio through α. In a uniaxial compression test ν_P as a function of α reads

$$\nu_P = -\frac{d_{P11}}{d_{P33}} = \frac{1/2 - [\alpha/3]^2}{1 + [\alpha/3]^2}. \tag{4}$$

Here, d_{P11} and d_{P33} refer to the components of the plastic rate of deformation tensor $\mathbf{d}_P$ in loading direction and transverse direction, respectively. Since $0 \leqslant \alpha^2 \leq 4.5$, for $\alpha = 0$ incompressible von Mises plasticity is recovered whereas for $\alpha = \sqrt{4.5}$ zero plastic Poisson's ratio is due.

The finite strain kinematics is resolved using multiplicative decomposition of the deformation gradient into elastic and plastic parts with $\mathbf{F} = \mathbf{F}_E \cdot \mathbf{F}_P$. The rotated Kirchhoff[2] stress is defined as $\boldsymbol{\tau} = K\mathrm{tr}(\mathbf{E}_E)\mathbf{1} + 2G\mathrm{dev}(\mathbf{E}_E)$ relative to the intermediate configuration where K is the bulk modulus and G is the shear modulus. The elastic logarithmic strain is defined as $\mathbf{E}_E = 1/2\,\log(\mathbf{F}_E^\top \cdot \mathbf{F}_E)$. Plastic flow relative to the intermediate configuration is formulated as $\mathbf{d}_P = \mathrm{sym}(\dot{\mathbf{F}}_P \cdot \mathbf{F}_P^{-1})$ where $\mathbf{w}_P = \mathrm{skw}(\dot{\mathbf{F}}_P \cdot \mathbf{F}_P^{-1}) = \mathbf{0}$ is assumed. Here, a normality rule is used with $\mathbf{d}_P = \dot{\epsilon}_P\,\partial\Phi/\partial\boldsymbol{\tau}$. Finally, Cauchy stress at the current configuration is defined as $\boldsymbol{\sigma} = 1/\det(\mathbf{F})\,\mathbf{R}_E \cdot \boldsymbol{\tau} \cdot \mathbf{R}_E^\top$ where $\mathbf{R}_E$ is computed using the polar decomposition $\mathbf{F}_E = \mathbf{R}_E \cdot \mathbf{U}_E$. The experiments reveal barreling, which is naturally understood as a consequence of friction at the load surfaces.[3] This is maximum for 120 nm samples and minimum for 50 nm samples. As a consequence, the irreducibility of the stress state to the uniaxial state forces one to use a numerical solution scheme with domain discretization in evaluation of the material constants. Inevitably, the friction coefficient becomes an additional process parameter which has to be identified. Thus, finite element models reproducing the individual compression tests were set up and run. A surface-to-surface contact method with finite sliding formulation models the load surface, using a Coulomb friction model with penalty-enforced constraints. For each model, an inverse constrained parameter optimization study was realized, minimizing the error (deviation-square) defined based on the normalized values of experimentally monitored central and surface extractions as well as force demand histories during upsetting. Equal weighting factors were applied to each constituent. Strain-rate dependence was not considered.

The optimization aimed at identifying the four hardening parameters K, τ_∞, m and n, the parameter α which controls the lateral extension and the friction coefficient μ_f. The modulus of elasticity was taken as fixed for each ligament size. For 50 nm sample 1300 MPa was used whereas for 150 nm and 180 nm samples 750 MPa was used. These values were obtained from experiments by measuring the unloading modulus at around 15% engineering strain. The effect of the variation of the density on the change of the macro elasticity modulus was not accounted for.

4. Results

Preliminary to the discussion of representative experimental results we note that reproducibility was verified through the

[1] The following notations will be used. Assuming $\mathbf{a}, \mathbf{b}$, and $\mathbf{c}$ as three second order tensors, together with Einstein's summation convention on repeated indices, $\mathbf{c} = \mathbf{a} \cdot \mathbf{b}$ represents the single contraction product with $c_{ik} = a_{ij}b_{jk}$. $d = \mathbf{a} : \mathbf{b} = a_{ij}b_{ij}$ represents the double contraction product, where d is a scalar. $\mathrm{dev}(\mathbf{a}) = \mathbf{a} - 1/3\mathrm{tr}(\mathbf{a})\mathbf{1}$ and $\mathrm{tr}(\mathbf{a}) = a_{ii}$ stand for the deviatoric part of and the trace of $\mathbf{a}$, respectively, with $\mathbf{1}$ denoting the identity tensor. $\mathrm{sym}(\mathbf{a})$ and $\mathrm{skw}(\mathbf{a})$ denote the symmetric and the skew-symmetric parts of $\mathbf{a}$. $\mathbf{a}^\top$ and $\mathbf{a}^{-1}$ respectively represent the transpose and the inverse of $\mathbf{a}$ whereas $\det(\mathbf{a})$ and $\log(\mathbf{a})$ denote the determinant and the natural logarithm, respectively. $\dot{\mathbf{a}}$ gives the material time derivative of $\mathbf{a}$.

[2] Since the material model accounts for high compressibility, overall formulation is made with respect to the intermediate configuration and using the (rotated) Kirchhoff stress tensor rather than Cauchy stress tensor similar to, e.g., [26]. This causes relative density dependence in Cauchy stress response throughout an applied loading path. Hence a compression–tension asymmetry in plastic response is inherently accounted for.

[3] Irrecoverable material deformation in lateral direction is con- trolled by both friction and plastic Poisson's ratio. For zero plastic Poisson's ratio, a nonzero friction does not cause bulging. On the other hand for zero friction in addition to nonzero plastic Poisson's ratio, lateral deformation occurs but uniformly throughout the specimen axis.

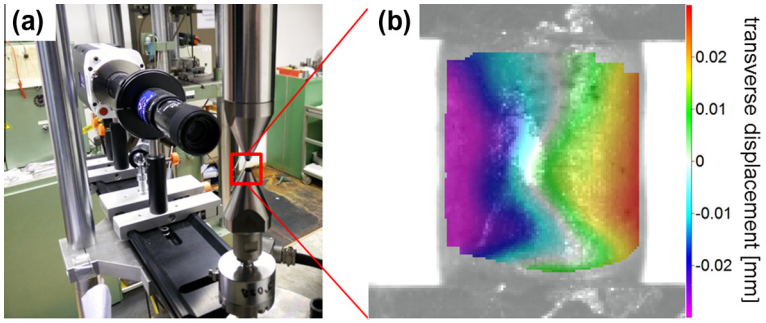

Fig. 1. Deformation experiments. (a) Test set up. Steel punches and camera with microscope are depicted. (b) Transverse displacement map for the example of npg with a ligament size of 180 nm at 35% engineering strain.

investigation of overall 18 samples, and that the trends for ν_E and ν_P as well as the numerical values presented are consistent between all experiments.

The bold lines in Fig. 2 show experimental results for the dependence of stress (Fig. 2a) and of transverse strains (Fig. 2b and c) at different positions on the axial engineering strain. The stress–strain behavior is well compatible with previous reports [11,13,21,24], specifically in respect to the high deformability, the pronounced strain hardening, and the trend for more strength at smaller values of the ligament size, L. Also, in each case the transverse strain in the sample center (b) exceeds the value of the transverse strain at the contact area (c). This effect is significantly more pronounced for samples with larger ligament sizes. It testifies to a finite plastic Poisson's ratio along with friction at the contact area and manifests itself visually in the form of barreling.

In Fig. 3, symbols represent the evolution of the two Poisson's ratios as determined from the experiment via Eq. (1). Part (a) of the figure shows ν_E, based on the load/unload tests. We find ν_E essentially independent of L, starting out at $\nu_E = 0.20 \pm 0.02$ for the undeformed material and increasing weakly as the sample is densified during plastic compression.

The symbols in Part (b) of Fig. 3 show our experimental results for ν_P. Nonzero values are found, and the sample with $L = 50$ nm exhibits a significantly lesser initial ν_P (~ 0.08) compared to the samples larger L (~ 0.18).

FEM simulation results were matched to the experimental data of Fig. 2a–c, varying the parameters for the Deshpande–Fleck model for best fit as explained above. The FEM results, shown superimposed to the compression test data in Fig. 2, are in remarkable agreement with the experiment. Table 1 lists the refined values of the parameters. The α-values suggest plastic Poisson's ratios via Eq. (4); this yields $\nu_P = 0.078$, 0.178 and 0.164 for $L = 50$, 120 and 180 nm, respectively. Comparing this data, see solid lines in Fig. 3, to the direct experimental results for ν_P shows excellent agreement at small strains. While the Deshpande–Fleck model's assumption of a fixed ν_P results in a failure to capture the experimental observation of a gradual increase in transverse coupling strength during compressive plastic densification, the agreement between model and experiment at small strains supports the validity of that data.

5. Discussion

To start out we inspect the dependence of the elastic parameters of isotropic metal networks, such as NPG, on their solid fraction φ. Isotropic elasticity has only two independent elastic parameters, and a specific consequence is that $\nu_E = 1/2 - 3G/[2G + 6K]$. Note that, as a result of the different scaling of the axial-versus the bending-stiffness of beams with

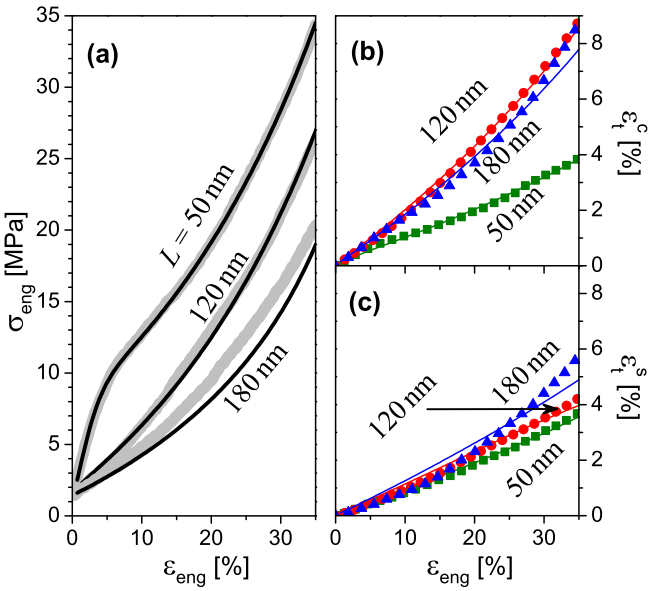

Fig. 2. Single loading compression tests of nanoporous gold with varying ligament size, experimental (bold lines and symbols) and finite element results (lines): (a) engineering stress σ_{eng}, (b) transverse engineering strain in the sample center ε_t^c and (c) transverse engineering strain at the contact area ε_t^s, all plotted vs. the engineering strain in loading direction ε_{eng}. Stress offset at zero strain is due to the applied pre-load.

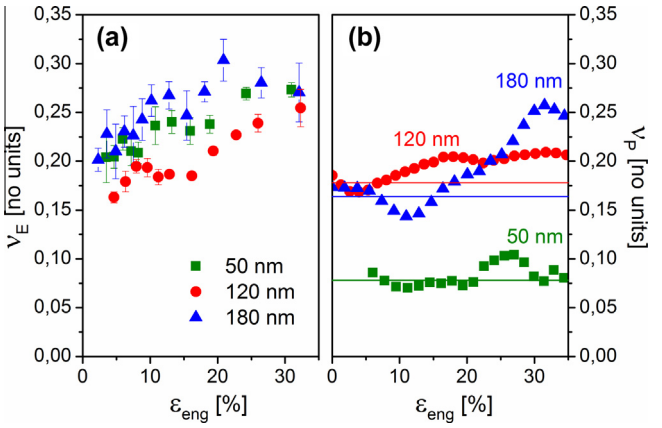

Fig. 3. Experimental data for the two different Poisson's ratio's versus the engineering strain ε_{eng}. (a) Elastic Poisson's ratio ν_E measured during unloading. (b) Plastic Poisson's ratio ν_P from direct experimental analysis (symbols) and from fitting the parameters in the Deshpande–Fleck constitutive equation during FEM simulation of the experiment (lines). Note the good agreement at small strains.

Table 1
Plastic hardening parameters obtained by fitting the constitutive model to the experiment through the intermediate of finite-element modeling. Meaning of symbols: L – mean ligament diameter, K – linear hardening coefficient, τ^{∞} – saturation stress, m – hardening exponent 1, n – hardening exponent 2, α – yield surface ellipticity, μ_f – friction coefficient.

L (nm)	K (MPa)	τ^{∞} (MPa)	m (–)	n (–)	α (–)	μ_f (–)
50	35.074	7.895	139	1.307	$\sqrt{3.52}$	0.004
120	37.809	1.993	15.261	0.561	$\sqrt{2.46}$	0.067
180	25.886	26.08	4.495	4.998	$\sqrt{2.60}$	0.045

the beam diameter, the values of elastic constants relating to bending-dominated deformation modes tend to scale quadratically with φ, whereas axial deformation gives a linear scaling [18].

In the spirit of a qualitative argument we can hypothesize that shear tends to emphasize bending, so that G varies as $G = c_G\varphi^2$. Hydrostatic loading, on the other hand, tends to favor either, bending or compression, depending on the degree of order. For network structures with a high degree of local order, the short-range order along each node of the network resembles that of periodic lattices. For NPG, the gyroid and diamond lattices of Refs. [18,20] may be considered in this sense. This is significant since, for a sufficiently symmetric lattice, isotropic compression or expansion simply changes the lattice parameter, leaving the angles between the connecting beams in the unit cell invariant. This is a purely axial deformation mode for each beam, implying a linear variation of K with φ in networks with high local symmetry. The gyroid lattice, as an example, indeed has $G \propto \varphi^2$ and $K \propto \varphi$ [18]. On the other hand, breaking the periodicity by introducing disorder in the lattice will result in a more general reaction to hydrostatic load, with a mixture of bending and stretching. We may therefore take $K = c_K\varphi^k$ with the value of the exponent k somewhere in-between the extremes 1 (for locally ordered structures) and 2 (for disorder).

Recalling the link between the elastic parameters of isotropic solids, we find that

$$\nu_E = \frac{1}{2} - \frac{3c_G}{2c_G + 6c_K\varphi^{k-2}}. \quad (5)$$

It follows that, within our assumptions, $k = 2$ of the disordered network gives ν_E independent of φ and smaller than 1/2. By contrast, $k = 1$ in the limit of high symmetry and order results in a density-dependent ν_E that approaches 1/2 in the limit of small φ. In other words, the elastic Poisson's ratio of network solids with low density diminishes with increasing disorder.

Turning now to experiment, Fig. 4 shows published data for the elastic and plastic Possion's ratios of NPG alongside the results of the present work (in their limit of small deformation, in the interest of comparability). It can be seen that the ν_E from the various sources are in good agreement, and specifically the results suggest that ν_E is independent of the ligament size. Combining the present data and that from Refs. [6,15] yields $\nu_E = 0.18 \pm 0.03$. Remarkably, this is significantly less than what is found for conventional metallic foams, for which typically ν_E is in the range of 0.31–0.34 [17].

In their analysis of an FEM study, Huber et al. [20] advertised the impact of disorder on the mechanical properties of network solids. In agreement with our reasoning, their model indeed shows that disorder diminishes ν_E, reproducing the experimental $\nu_E \approx 0.18$ if the disorder parameter A, defined as the mean square displacement of the nodes from the lattice sites of the diamond beam structure, takes the value $A = 0.3$. This is similar to $A = 0.4$ that Huber et al. [20] find to best reproduce the stiffness of experimental NPG. The results by Khaderi et al. [18] for the ordered gyroid lattice imply $\nu_E = 0.33 \pm 0.01$ for the interval of solid fractions, $\varphi = 0.25 - 0.28$, of the present experiments. In spirit of our discussion of the role of disorder, the smaller value of the experiment is consistent with the deviation from perfectly crystalline order in the network of NPG.

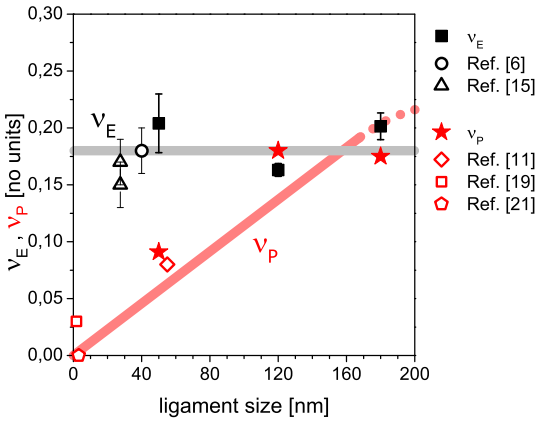

Fig. 4. Elastic (black) and plastic Poisson's ratio (red) at low elastic and plastic strain, respectively, plotted vs. the ligament size. (For interpretation of the references to colour in this figure legend, the reader is referred to the web version of this article.)

Quite contrary to the elastic Poisson's ratio, our results for the plastic Poisson's ratio in Fig. 4 suggest a significant dependence the ligament size. This trend becomes even more significant when results from previous experimental [11,13] studies are included. In fact, if the trend is taken at face value, then it reconciles the near zero ν_P of the molecular dynamics studies [19,21], which explore extremely small L, with the finite ν_P of the experiments at lager L. This is apparent as the straight line through the origin, displayed in Fig. 4 to emphasize the trend in the ν_P, is well compatible with all findings. Thus, a strong variation of ν_P with L may explain why different studies arrived at such different conclusions on the magnitude of the transverse contraction.

Similar to ν_E, the experiments find ν_P to increase slightly with proceeding densification. Reproducing this trend in the constitutive framework of Deshpande and Fleck would require that α is allowed to vary with φ.

A remarkable finding from the FEM model is that the friction coefficients are very low compared to what is known for the kinetic friction coefficient of gold in contact with steel, which ranges from 0.4 to 0.5 [27]. As friction is of technological interest in many scenarios, the friction behavior of nanoporous metals might deserve a closer study.

6. Conclusions

Our study of the transverse mechanical coupling of nanoporous gold during compressive loading, combining experiment with finite element modeling, finds the elastic Poisson's ratio independent of the ligament size. As the sample densifies during compression, ν_E increases slightly, from initially around 0.20 to near 0.3. We present an argument that links the low initial value of ν_E, as compared to predictions from lattice-based models for network solids, to disorder in the ligament network of nanoporous gold. This notion confirms the suggestion by Huber et al. [20] of the important impact of disorder on the mechanical properties of network solids.

When combined with literature data from experiments and atomistic modeling, our results suggest the plastic Poisson's ratio to scale with the ligament size, L. As the scaling implies vanishing ν_P in the limit of vanishing L, the observation is, specifically, consistent with the finding of near zero transverse plastic strain in compression during atomistic simulation studies, which are restricted to samples with small L.

Our work finds the Deshpande–Fleck model in good agreement with experimentals. This finding is remarkable since it demonstrates for the first time that the deformation of nanoporous gold can be modeled using a fully homogenized constitutive law.

Acknowledgment

This work was supported by DFG via SFB 986 "M^3", sub-projects B2 and B6.

References

[1] J. Weissmüller, R.C. Newman, H.-J. Jin, A.M. Hodge, J.W. Kysar, MRS Bull. 34 (2009) 577.
[2] A.M. Hodge, T. John Balk, in: Nanoporous Gold: From an Ancient Technology to a High-Tech Material, The Royal Society of Chemistry, 2012, pp. 51–68.
[3] J. Biener, A.M. Hodge, J.R. Hayes, C.A. Volkert, L.A. Zepeda-Ruiz, A.V. Hamza, F.F. Abraham, Nano Lett. 6 (2006) 2379–2382.
[4] J. Biener, A.M. Hodge, A.V. Hamza, Appl. Phys. Lett. 87 (2005) 121908.
[5] R. Li, K. Sieradzki, Phys. Rev. Lett. 68 (1992) 1168–1171.
[6] S. Sun, X. Chen, N. Badwe, K. Sieradzki, Nat. Mater. 14 (2015) 894–898.
[7] J. Biener, A.M. Hodge, A.V. Hamza, L.M. Hsiung, J.H. Satcher, J. Appl. Phys. 97 (2005).
[8] A. Hodge, J. Biener, J. Hayes, P. Bythrow, C. Volkert, A. Hamza, Acta Mater. 55 (2007) 1343–1349.
[9] A. Hodge, R. Doucette, M. Biener, J. Biener, O. Cervantes, A. Hamza, J. Mater. Res. 24 (2009) 1600–1606.
[10] C.A. Volkert, E.T. Lilleodden, D. Kramer, J. Weissmüller, Appl. Phys. Lett. 89 (2006).
[11] H.J. Jin, L. Kurmanaeva, J. Schmauch, H. Rösner, Y. Ivanisenko, J. Weissmüller, Acta Mater. 57 (2009) 2665–2672.
[12] H.-J. Jin, J. Weissmüller, Science 332 (2011) 1179–1182.
[13] K. Wang, J. Weissmüller, Adv. Mater. 25 (2013) 1280–1284.
[14] D. Lee, X. Wei, X. Chen, M. Zhao, J. Hone, E.G. Herbert, W.C. Oliver, J.W. Kysar, Scr. Mater. 56 (2007) 437–440.
[15] T.J. Balk, C. Eberl, Y. Sun, K.J. Hemker, D.S. Gianola, JOM 61 (2009) 26–31.
[16] K. Wang, A. Kobler, C. Kübel, H. Jelitto, G. Schneider, J. Weissmüller, NPG Asia Mater. 7 (2015) e187.
[17] M. Ashby, A. Evans, N. Fleck, L. Gibson, J. Hutchinson, H. Wadley (Eds.), Metal Foams, Butterworth-Heinemann, Burlington, 2000.
[18] S.N. Khaderi, V.S. Deshpande, N.A. Fleck, Int. J. Solids Struct. 51 (2014) 3866–3877.
[19] D. Farkas, A. Caro, E. Bringa, D. Crowson, Acta Mater. 61 (2013) 3249–3256.
[20] N. Huber, R.N. Viswanath, N. Mameka, J. Markmann, J. Weimüller, Acta Mater. 67 (2014) 252–265.
[21] B.-N.D. Ngô, A. Stukowski, N. Mameka, J. Markmann, K. Albe, J. Weissmüller, Acta Mater. 93 (2015) 144–155.
[22] J. Biener, A. Hamza, A. Hodge, in: F. Yang, J.C. Li (Eds.), Micro and Nano Mechanical Testing of Materials and Devices, Springer, US, 2008, pp. 118–135.
[23] V.S. Deshpande, N.J. Fleck, Mech. Phys. Sol. 48 (2000) 1253–1283.
[24] N. Mameka, J. Markmann, H.-J. Jin, J. Weissmüller, Acta Mater. 76 (2014) 272–280.
[25] H.-J. Jin, S. Parida, D. Kramer, J. Weissmüller, Surf. Sci. 602 (2008) 3588–3594.
[26] I. Borja Ronaldo, C. Tamagnini, Computer Meth. Appl. Mech. Eng. 155 (1998) 73–95.
[27] K. Holmberg, A. Matthews, Coatings Tribology: Properties, Mechanisms, Techniques and Applications in Surface Engineering, Trib. Interf. Eng., Elsevier Science, 2009.